submitted to *Geophys. J. Int.*

InSAR observations and models of crustal deformation due to a glacial surge in Iceland

A. Auriac[1,5⋆], F. Sigmundsson[1], A. Hooper[2], K. H. Spaans[2], H. Björnsson[1], F. Pálsson[1], V. Pinel[3], K. L. Feigl[4]

[1] *Nordic Volcanological Center, Institute of Earth Sciences, University of Iceland, Sturlugata 7, 101 Reykjavík, Iceland*

[2] *School of Earth and Environment, University of Leeds, LS2 9JT, United Kingdom*

[3] *ISTerre, Université de Savoie, IRD, 73376 Le Bourget du Lac, France*

[4] *Department of Geosciences, University of Wisconsin-Madison, 1215 West Dayton Street, Madison WI 53706, USA*

[5] *Now at: Department of Geography, Durham University, South Road, Durham, DH1 3LE, UK*

SUMMARY

Surges are common at all the major ice caps in Iceland. Ice masses of gigatons may shift from the upper part of the outlet glacier towards the terminus in a few months, advancing the glacier front by up to several kilometres. The advancing ice front may be up to 100 m thick, increasing the load on crustal rocks correspondingly. We use the observed change in crustal loading during a surge of the western part of the Vatnajökull ice cap, Iceland, during 1993–1995 and the corresponding elastic crustal deformation, surveyed with interferometric synthetic aperture radar, to investigate the material properties of the solid Earth in this region. Crustal subsidence due to the surge reaches ∼75 mm at the edge of the Síðujökull outlet glacier. This signal is mixed with a broad uplift signal of ∼12 mm/yr, relative to our reference area, caused by the ongoing retreat of Vatnajökull in response to climate change. We disentangle the two signals by linear inversion. Finite element modelling is used to investigate the elastic Earth response of the surge, as well as to confirm that no significant viscoelastic deformation occurred as a consequence of the surge. The modelling leads to estimates of the Young's modulus and Poisson's ratio of the underlying Earth. Comparison between the observed and modelled deformation fields is made using a Bayesian approach that yields the estimate of a probability distribution for each of the free parameters. Residuals indicate a good agreement between models and observations. One-layer elastic models result in a Young's modulus of 43.2–49.7 GPa (95% confidence) and Poisson's ratio of 0–0.27, after removal of outliers. Our preferred model, with two elastic layers, provides a better fit to the whole surge signal. This model consists of a one-kilometre-thick upper layer with an average Young's modulus of 12.9–15.3 GPa and Poisson's ratio of 0.17, overlying a layer with an average Young's modulus of 67.3–81.9 GPa and Poisson's ratio of 0.25.

Key words: Satellite Radar Interferometry - InSAR – Glaciology – Elastic deformation – Glacial surge – Numerical solutions – Young's modulus – Poisson's ratio.

1 INTRODUCTION

Glaciers cover 11% of Iceland (Fig. 1) (Björnsson 1978). Since they are currently retreating, widespread uplift induced by their melting occurs over a large area of Iceland. This uplift signal, reaching up to 20–25 mm/yr around the Vatnajökull ice cap, has been studied in detail over the past 20 years, to infer some of the properties of the underlying Earth, such as the thickness of the elastic crust and the viscosity of the underlying material (e.g., Pagli et al. 2007; Árnadóttir et al. 2009; Auriac et al. 2013). However, the Young's modulus E and Poisson's ratio v remain uncertain. Since crustal behaviour is mostly elastic at short time scales, these two elastic parameters control the upper Earth's layer deformation in response to sudden stress perturbations. Quantitative estimates of E and v are thus required to infer stress variations from surface deformations, e.g. due to fault unloading or magma pressurization. Most of the available estimates of the Young's modulus and Poisson's ratio are derived from seismic wave velocities (e.g., Allen et al. 2002). The parameters, inferred from the rapid dynamic response to passing seismic waves, are called dynamic values. Seismic studies provide detailed maps of the spatial variation of the Young's modulus, and how it increases with depth (Pálmason 1971; Gudmundsson 1988; Allen et al. 2002; Currenti et al. 2007; Hooper et al. 2011). In contrast, the static values of

⋆ E-mail: ama3@hi.is / a.m.auriac@durham.ac.uk

the parameters correspond to a static load. They can be measured in laboratory experiments (Cheng & Johnston 1981; Eissa & Kazi 1988; Asef & Najibi 2013) for a given range of confining pressure. They can also be estimated from modelling of the deformation signal induced by well-constrained surface loading perturbations, such as annual ice thickness variations (Grapenthin et al. 2006; Pinel et al. 2007). Comparative studies have shown that there is a difference between the dynamic and the static estimates of the Young's modulus, with a static-to-dynamic ratio (E_s/E_d) in the range 0.4–1.0 (Cheng & Johnston 1981; Asef & Najibi 2013). This ratio is highly dependent on the heterogeneity of microscopic structures of the rock material and its porosity, such that the difference tends to decrease with confining pressure. It follows that the estimate of static parameters from the dynamic ones is not straightforward and there is a need to provide good static in-situ estimates.

The aim of this study is to use interferometric synthetic aperture radar (InSAR) measurements to measure surface deformation associated with a glacial surge, and to model the observed deformation to constrain the elastic properties of the Earth. Surges are common at the outlet glaciers of all the major ice caps in Iceland (e.g., Thorarinsson 1969; Björnsson et al. 2003). Ice-flow at surge-type outlet glaciers is generally too slow to remain in balance with their accumulation rates. As a result, the glacier thickens in its upper part, thins and steepens in the lower part, and the terminus draws back. After several years of glacier surface steepening, the basal sliding velocity increases in a zone centred in the upper ablation area where crevasses are formed. Downstream from this zone of enhanced velocity, a step-like thickening of the glacier develops and a bulge, usually tens of metres high, advances at rates of 20–80 m per day. Propagation of the bulge to the glacier terminus generally requires less than a year. Once the bulge reaches the terminus, the glacier begins to advance as a vertical front, usually 20-50 m high. The maximum advance rate measured during a surge in Iceland was 100 m in 24 hours at the ice front of Brúarjökull outlet glacier (located in the northern part of Vatnajökull ice cap) in 1963. The large outlets of Vatnajökull typically advance about 1 km. The advance of the terminus may take several months. Surges alter the geometry of the ice caps, typically thinning the accumulation area by 25-100 m, reducing ice-surface slopes, and increasing glacier surface area and ice thickness at the terminus. Lingering effects of a surge can often be detected in the accumulation area in the form of crevassing and surface lowering several years after the terminus has stopped advancing. Following that, a quiescent phase takes over, building up to a new surge. Major surges, with return intervals of several decades, have occurred in all the large lobate outlets of Vatnajökull.

In this study, we map crustal deformation using InSAR data, which provide deformation observations with high spatial resolution. SAR acquisitions from May–October, 1993–2002 are used to measure the crustal deformation induced by a surge that occurred in 1993–1995 at the four major outlet glaciers of western Vatnajökull (Fig. 1). We use the finite element method to model the surge-induced crustal deformation and compare it to the InSAR observations. This allows us to estimate the effective Young's modulus, E, and Poisson's ratio, v, of the Icelandic crust/mantle.

2 GLACIAL SURGE HISTORY

The glacial surge we study took place in 1993–1995 at neighbouring outlet glaciers of western Vatnajökull: Síðujökull, Tungnaárjökull, Skaftárjökull and Sylgjujökull (Fig. 1). The first indications of a surge of Síðujökull were the formation of crevasses in 1990 in the accumulation area. In January 1994, a $\sim$70 m high bulge was observed moving down-glacier, and 4 months later, the surge was over, affecting an area of 500 km^2 and resulting in an advance of the glacier terminus by 1,150 m. On Tungnaárjökull, increased ice velocities were first detected in 1992–1993 and in late 1994 a bulge started to propagate downwards. The surge was finished in mid-1995, moving the terminus forward by about 1,200 m. The surface drawdown in the reservoir area extended 30 km up-glacier from the terminus. On both outlets the reservoir area lowered by 10–80 m, and the terminus thickened in excess of 100 m (more details in Björnsson et al. 2003). Skaftárjökull and Sylgjujökull surged in 1994–1995.

The redistribution of the ice mass during the surges of western Vatnajökull (Fig. 2) was estimated by differencing surface maps of the glaciers from 1993 and 1995. Digital elevation models (DEMs) for 1993 and 1995 were constructed by adjusting four basic maps available prior to and after the surge (from 1980, 1990, 1995 and 1998) with the help of observed spatial surface elevation changes, i.e. a time series of annual in situ GPS surveys at several scattered points over the glaciers in the 1980s and 1990s. We assumed that the main topographic forms of the glacier surface, shown in the 1980's and 1990/91 DEMs, remained unchanged until the surges in 1993. Likewise, we assume the maps of 1995 and 1998 display the shape of the glacier surface after the surges in 1995. The 1980 DEM was created from digitized elevation contour lines of the DMA series 1:500,000 paper maps (DMA series C761 produced by the Defence Mapping Agency Hydrographic/Topographic Center (DMAHTC), Washington DC) constructed from aerial photographs. The point elevation accuracy in this DEM is estimated to be $\sim$5 m. The 1990–91 map was produced from precision barometric altimetry profiles about 1 km apart, with point accuracy of 2 m (Björnsson & Pálsson 1991; Björnsson et al. 1992). A DEM of the terminus and lowest part of Tungnaárjökull was extracted from aerial photography survey in late summer 1995, point elevation accuracy $\sim$2 m. Finally, a DEM was derived by an airborne EMI-SAR survey in 1998 (Magnússon et al. 2004), with estimated 1 m accuracy. We estimate uncertainty in the regional elevation difference between the DEMs from 1993 and 1995 to be 2–5 m. The volume of ice transferred in the surges, calculated as the difference between the 1993 and 1995 DEMs is estimated at 16$\pm$1 km^3, corresponding to $\sim$15 Gt$_{we}$ (water equivalent) assuming an average ice density of 917 kg/m^3. We assume here that there were no changes in the snow and firn layers on the ice cap and that the ice density remained constant before, during and after the surge.

3 INSAR OBSERVATIONS

We used 27 acquisitions from the European Space Agency's ERS-1 and ERS-2 synthetic aperture radar satellites, descending track 9, captured over the southwestern part of Vatnajökull ice cap between 1993 and 2002 (Fig. 1). We processed the SAR acquisitions in a similar way as Auriac et al. (2013), using the Repeat Orbit Interferometry PACkage (ROI-PAC) (Rosen et al. 2004) to focus the raw data, and the Delft Object-oriented Radar Interferometric Software (DORIS) (Kampes & Usai 1999) to form the interferograms. The small baseline approach from the Standard Method for Persistent Scatterers (StaMPS) (Hooper 2008) package was used to form interferograms from various pairs of images for which the differences in perpendicular and temporal baselines are small. From these, we selected 65 highly coherent interferograms (Fig. 3), formed from 24 of the 27 original SAR acquisitions (Table 1). Finally, we cropped the scene to keep only the region surrounding the outlet glaciers, and resampled the coherent pixels to a 500 m grid. We also removed the points located on the ice cap and outliers (noisy points located along the lake and rivers in the west of the scene), leaving 2455 data points in total.

The deformation observed in the interferograms is in the line-of-sight (LOS) direction between the satellite and the ground, which deviates $\sim$23° from vertical, as the radars are side-looking. The LOS unit vector, in the direction from ground to satellite, is approximately (-0.35, -0.10, +0.90) in east, north and up components. As the surge-induced crustal deformation is dominated by vertical movement (see Section 7), and InSAR is most sensitive to the vertical direction, the signal observed in the interferograms relates mostly to a vertical change corresponding to a subsidence. It is generally possible to separate the horizontal east-west deformation component from the vertical one by using SAR images acquired in both ascending and descending mode. However, due to the lack SAR data acquired in ascending configuration over the study area, this could not be achieved here. Only the crustal deformation from the surge at Síðujökull, Skaftárjökull and the southern part of Tungnaárjökull outlet glaciers is observed, as the InSAR data we use do not cover the margins of Sylgjujökull and the northern part of Tungnaárjökull outlet glaciers.

3.1 Surge signal and time series of interferograms

Interferograms spanning the year 1994 reveal a clear LOS lengthening signal associated with the glacial surge. Fig. 4 shows an example of such an interferogram, both wrapped and unwrapped, with maximum subsidence of $\sim$70–80 mm observed at the ice margin, relative to a reference area located at a distance of $\sim$15 km from the ice edge, in the bottom right corner of the InSAR scene. The reference area was chosen far away from the ice cap not to be influenced by the surge-induced crustal deformation. The surge signal decays rapidly away from the ice cap, with only $\sim$15 mm subsidence observed at $\sim$6 km from the ice edge. We inverted the 65 small baseline interferograms using least-squares to give a single-master time series of 23 unwrapped interferograms using StaMPS (Fig. 5). It shows cumulative displacement through time with respect to the first image on 26 June 1993, relative to the reference area. Two signals are observed: (i) the LOS lengthening signal related to the surge, appearing in the first image after the surge (19 June 1995) and all subsequent images, and (ii) the LOS shortening deformation due to glacial isostatic adjustment (GIA), as described by Auriac et al. (2013) (i.e. the ground deformation occurring around Vatnajökull due to the general retreat of the ice cap over the past 120 years and seasonal changes in snow and ice cover), most clearly visible over the eastern half of the scene as time increases.

Contrary to the observations made by Sauber & Molnia (2004) for the surge of Bering Glacier, Alaska, in 1993–1995, the deformation signal associated with the drawdown of the reservoir area on Vatnajökull ice cap could not be observed by GPS due to a lack of GPS measurements on the nunataks at the time of the surge. The deformation of these nunataks could not be retrieved by InSAR data as it is nearly impossible to reliably unwrap between the stable points outside the ice cap and the clusters of isolated stable points on nunataks.

3.2 Disentangling surge and GIA signals

The GIA and surge signals are both present in the 1993–2002 time series of interferograms. In order to model the surge separately, we first estimated the contributions of both signals for each pixel. Each signal has its own time frame, the GIA spanning the whole time series and the surge being a singular event spanned completely by a single pair of consecutive images, assuming the response of the surge is purely elastic (see Section 7). For a given pixel, the displacement as a function of time may therefore be modelled as a constant velocity (GIA) plus a step function (surge). Separating the two processes is achievable through least-squares inversion of the single-master time series data. The equation to solve for each pixel is

$$\mathbf{\Delta}\phi_{\mathbf{i}} = \mathbf{A}\mathbf{x}_{\mathbf{i}} \tag{1}$$

where $\mathbf{\Delta}\phi_{\mathbf{i}}$ is a vector with the phase value of the i^{th} pixel in each interferogram, $\mathbf{A}$ is a design matrix and $\mathbf{x}_{\mathbf{i}}$ is a vector of unknown parameters we invert for. In our case, the vector of unknowns includes, for each pixel, two parameters of interest: (i) the estimation of the ongoing GIA signal through time, $v_{GIA,i}$, which is assumed constant before and after the surge (see Section 7), and (ii) the estimate of the step displacement caused by the surge, $d_{surge,i}$. The vector also includes two nuisance parameters that need to be evaluated for each pixel: the estimate of atmospheric component from the master acquisition, $a_{m,i}$, and the estimate of the DEM error, which is related to the perpendicular baseline, $c_{topo,i}$. For the i^{th} pixel, equation (1) can be rewritten as

$$\begin{bmatrix} \Delta\phi_{i,1} \\ \vdots \\ \Delta\phi_{i,k} \\ \Delta\phi_{i,k+1} \\ \vdots \\ \Delta\phi_{i,n} \end{bmatrix} = \begin{bmatrix} \Delta t_1 & 1 & 0 & B_{perp_1} \\ \vdots & \vdots & \vdots & \vdots \\ \Delta t_k & \vdots & 0 & B_{perp_k} \\ \Delta t_{k+1} & \vdots & 1 & B_{perp_{k+1}} \\ \vdots & \vdots & \vdots & \vdots \\ \Delta t_n & 1 & 1 & B_{perp_n} \end{bmatrix} \begin{bmatrix} v_{GIA,i} \\ a_{m,i} \\ d_{surge,i} \\ c_{topo,i} \end{bmatrix} \tag{2}$$

where k is the index of the last interferogram before the surge, n is the total number of interferograms in the single-master time series, Δt is the time between the master and slave acquisitions, and B_{perp} the perpendicular baseline between the two acquisitions. We solved these equations for all the pixels and derived a vector with an estimate for the GIA and surge-induced crustal displacements, $\mathbf{v}_{GIA}$ and $\mathbf{d}_{surge}$, respectively.

We solved for the vector of unknown parameters using least-squares weighted by the inverse variance-covariance matrix of the data. To estimate the variance of each interferogram, we deramped a 34×19 km area at the southwest corner of the full InSAR scene, considered far from any signal, and calculated the variance of the phase of the selected pixels in this area for each interferogram of the single-master time series. We assumed the variance of this background signal to be representative of the complete scene. As the residual phase of the pixels in the interferogram is assumed to be uncorrelated in time, off-diagonal elements of the variance-covariance matrix were set to zero.

Fig. 6 shows the results of the least-squares inversion for the GIA and surge estimate, relative to a reference area at (-17.67°E, 63.97°N). The GIA signal, $\mathbf{v}_{GIA}$, has a maximum LOS shortening rate of up to 10–12 mm/yr at the ice margin east of Síðujökull outlet glacier, similar to the observations from

Auriac et al. (2013), while a maximum LOS lengthening of 70–75 mm is estimated for the surge step function, $\mathbf{d}_{surge}$.

4 MODELLING

4.1 General set-up

We modelled the elastic ground deformation caused by the surge with the finite element method, using the Abaqus commercial software (ABAQUS 2009). This method also allowed us to investigate the possibility of a viscoelastic response of the Earth to the glacial surge, and thus test the assumptions applied in the least-squares inversion (see Sections 3.2 and 7). We built the models following the same approach as Auriac et al. (2013), using a volume of $2000 \times 2000 \times 1000$ km in the east-west, north-south and depth dimensions, respectively. The same assumptions as mentioned by Auriac et al. (2013) stand, i.e. flat Earth, isotropic material, horizontal layering, and no plate spreading. The domain is large enough so that the fixed boundary conditions at the vertical and lower boundaries do not significantly affect the modelled displacements. Even though our model configuration approximates a half-space, we prefer the term layer to refer to each finite volume with similar elastic properties. A model where the entire volume has uniform properties will thus be called a one-layer model, and a model with two different uniform properties within the total volume will be called a two-layer model.

The ice model is based on the ice mass changes described in Section 2 and Fig. 2. In order to account for the large variations over short distances in the surge model, we modified the original mesh (of the Earth model) used by Auriac et al. (2013) at the surface such that, in the load region, nodes are located every $\sim$250 m. The mesh then becomes coarser with distance. More than 210,000 nodes are present at the surface. To implement the ice model in Abaqus, we searched for the surge model point closest to the centre of the mesh element's face at the surface, and assigned it the corresponding value, defined as a pressure load.

Two series of models were created. We first created one-layer elastic models with Poisson's ratio, *v*, ranging from 0.025–0.500 with steps of 0.025, and Young's modulus, *E*, of 20 GPa. In a purely elastic model, according to Hooke's law, the displacement X induced by a surface load F is inversely proportional to *E*, and can be expressed as

$$X = F/E \tag{3}$$

Since the same load (surge model) was applied in all our models, we can consider F as constant.

Using equation (3) and the predicted displacement for one value of E (20 GPa) from our modelling, we can calculate the surface deformation for any value of E by scaling. In our case, we calculated the deformation to E ranging from 5–100 GPa, for each value of v. To verify the numerical modelling, we ran a few extra models with v=0.25 and E=60 GPa and 90 GPa, and compared the displacements to those calculated by scaling. Fig. 7 shows the results of this comparison for one randomly chosen node of the mesh, indicating full consistency. In addition, we calculated analytical solutions for the surge displacement using the half-space Green's functions, by discretising the surge into point loads, applied to the centre of each element from the finite element mesh. This solution is based on the same ice model as the finite element models. The displacements (horizontal, U_r, and vertical, U_z) for a point surface load are

$$U_r(r) = -\frac{g}{2\pi}\frac{(1+v)(1-2v)}{E}\frac{1}{r} \tag{4}$$

and

$$U_z(r) = \frac{g}{\pi}\frac{1-v^2}{E}\frac{1}{r} \tag{5}$$

where r is the distance from the load, g is the acceleration of gravity, v the Poisson's ratio, and E the Young's modulus (e.g. Pinel et al. 2007). The total displacement at each of the mesh points is estimated by considering the total ice mass and adding up the displacement induced by each of the point loads, using v=0.25 and E=40 GPa. Model displacements for other values of E were found by scaling. The predicted displacement with this method was compared to those obtained from the finite element models (Fig. 7).

The second series of models corresponds to two-layer elastic models with a 1-km-thick upper layer. The mesh and ice model are the same as used for the one-layer elastic models. We used different values for the Poisson's ratio of each layer (v_1 for the top layer and v_2 underneath), using the best-fit value provided by the one-layer elastic models and more commonly used values for crustal rocks. The Young's moduli (E_1 for the top layer and E_2 underneath) were varied from 10–18 GPa with steps of 2 GPa for E_1, and from 55–90 GPa with steps of 5 GPa for E_2.

4.2 Estimating the Young's modulus and Poisson's ratio

We solved for the best-fitting values of E and v by comparing the deformation field calculated from the finite element models to the surge-induced LOS change estimated from the InSAR data. This was achieved using a statistical method based on Bayes' rule, similar to that used by Hooper et al. (2013) and Auriac et al. (2013). The approach used here though is simpler, because no GPS data are used in the comparison between the observed surge-induced and modelled deformation fields. We calculated the weighted residual sum of squares, WRSS, as

$$WRSS = (\mathbf{d} - \mathbf{G}(\mathbf{m}))^T \mathbf{Q}^{-1} (\mathbf{d} - \mathbf{G}(\mathbf{m})) \tag{6}$$

where $\mathbf{d}$ is the vector of observations, $\mathbf{m}$ is the vector of model parameters, $\mathbf{G}(.)$ is the model function that maps the model parameters to the observations, and $\mathbf{Q}$ is the variance-covariance matrix of the InSAR observations, which are highly correlated in space.

The variance-covariance matrix accounts for residual atmospheric, decorrelation and unwrapping errors. It was estimated by a bootstrapping approach based on the one described by Auriac et al. (2013) but accounting for the following improvements. We ensured here that interferograms from both before and after the surge were sampled during each realisation of the bootstrap. To ensure the estimate of the covariance includes the background noise only, we removed our estimate of d_{surge} (calculated using weighted least-squares) from each estimate of the surge obtained during bootstrapping. For 500,000 random pairs of points, we then calculated the semi-variogram as the variance of the difference of value of the residual d_{surge} between the two points in each pair. The semi-variogram was then binned according to the distance between the points and fitted with an exponential variogram function, from which the covariance function was calculated. The diagonal elements were set to a constant ($\sim$20.7 mm^2), corresponding to the zero lag covariance which includes a nugget value (estimated as the semi-variogram value at zero lag).

Residuals, $\mathbf{d} - \mathbf{G}(\mathbf{m})$, were calculated for each discrete value of the model parameters and interpolated in between to derive the posterior probability distribution of the model parameters. For each set of residuals, we estimated and removed a plane which accounts for orbital effects (residual orbit signals resembling a bilinear ramp) and for the systematic offset between the relative LOS InSAR observations and the absolute model displacements.

From equation (6) and according to Bayes' rule, the posterior probability can be estimated using

$$p(\mathbf{m}|\mathbf{d}) = K \frac{\sigma^{-n}}{\sqrt{(2\pi)^n |\mathbf{Q}|}} \exp\left[-\frac{WRSS}{2\sigma^2}\right] \tag{7}$$

where K is a constant, σ is a scaling factor of the variance-covariance matrix to account for model errors, and n is the number of pixels. We set K in such a way that the total probability equals unity. We then determined the uncertainty region of our parameters as the area containing 95% of the total probability. The dimensionless scaling factor σ is constant for all combinations of model parameters within one series of models (one-layer elastic or two-layer elastic models), and was independently calculated from the best WRSS estimate for each model series such that $WRSS/\sigma^2 = n$. It varied from 2.2 to 2.7 depending on the model used.

5 ALTERNATIVE APPROACH USING GIPHT

The General Inversion for Phase Technique, GIPhT, (Feigl & Thurber 2009; Ali & Feigl 2012) has also been applied to the surge data from western Vatnajökull ice cap. The approach used two wrapped interferograms created from four SAR acquisitions from the ERS-1 and 2 satellites, track 9. They span similarly long time intervals over 1993–1995 and 1998–2000. Assuming that the GIA signal is constant with time (see Section 7), we subtracted the later interferogram from the first one to remove the GIA deformation, providing an estimate of the surge displacement. The observed subsidence is more than one fringe (more than 28 mm of range change) in most areas and nearly two fringes close to the eastern edge of Síðujökull outlet glacier ($\sim$56 mm of range change) within $\sim$10 km from the ice edge. This is consistent with what is observed in Fig. 6b.

We modelled this estimate of surge deformation with the Green's function approach (Eqs. 4 and 5). For each pixel, the calculation convolves the map of the inferred mass redistribution of ice from the surge (Fig. 2) with the Green's function.

Consequently, we can estimate the Young's modulus *E* and Poisson's ratio *v* of the rocks around the glacier by minimizing the residual between the observed and modelled values of the InSAR phase. To solve this inverse problem, we applied the GIPhT method as described by Feigl & Thurber (2009) and Ali & Feigl (2012).

6 RESULTS

Results of the comparison between the surge displacement field estimated from the least-squares inversion ($\mathbf{d}_{surge}$) and our finite element models (both one-layer and two-layer elastic) are presented in Figs. 8 to 11 and Table 2. The deformation patterns from the InSAR observations and the models are very similar. The magnitude of crustal deformation around the surging outlet glaciers, as well as the extent and decay of the signal away from the ice margin are well reproduced by the models, indicating high quality of the ice model and applicability of the Earth models.

Comparison between the one-layer elastic models and the surge-induced crustal LOS displacement ($\mathbf{d}_{surge}$) are displayed in the top row of Fig. 8, showing $\mathbf{d}_{surge}$ from which the ramp and offset estimated during the Bayesian approach have been removed, the best-fit model, and the residuals between the two. The residual plot shows that, although the best one-layer elastic model manages to predict quite well the pattern of deformation, it does not accurately reproduce the deformation within 5 km of the ice edge, where residuals can reach 26–28 mm. The model cannot simultaneously reproduce both the gradient of deformation in the near-field (1–2 km from the edge) and far-field, which requires a higher value. This compromise model results in the relatively low estimate of the Young's modulus, E=46.4$^{+3.3}_{-3.2}$ GPa, shown in the probability estimate in Fig. 9 and in Table 2. The maximum posterior probability estimate for the Poisson's ratio is 0.17, but the probability distribution function (Fig. 9) shows that this parameter is barely constrained by these data, and the 95% confidence interval spans 0–0.27. The GIPhT method, solving for the average value of the free parameters over a half-space, finds a Young's modulus of E=64.0± 6 GPa and a Poisson's ratio of v=0.36± 0.06. It seems this methods finds a good fit to the far-field deformation, explaining the difference with the Bayesian approach. From the results of our one-layer elastic models, we conclude that the crustal deformation pattern from the glacial surge cannot be adequately fit with a simple one-layer model.

In order to fit both the near- and the far-field displacements, a more complex model is needed. For this purpose, we ran the two-layer elastic models, solving for the best-fit Young's modulus of each layer (E_1 for the top layer and E_2 underneath). The 1-km-thick top layer, with a relatively low Young's modulus, is used to account for the large subsidence observed in the near-field region, while the underlying layer, with an overall higher Young's modulus, is needed to accommodate the far-field deformation. The 1 km thickness of the top layer was chosen according to the fact that the near-field gradient of deformation, outlined with the one-layer elastic models, is only observed with 1–2 km from the ice edge. We used three different combinations of the Poisson's ratios (v_1 for the top layer and v_2 underneath): (i) both v_1 and v_2 are set to 0.25, as it is a commonly assumed value for the Poisson's ratio of crustal rocks; (ii) we use v_1=0.17, as predicted by the one-layer models, and v_2=0.25; and (iii) both v_1 and v_2 are set to 0.17. Results from the Bayesian approach are presented in Fig. 10 and best-fit estimates of E_1 and E_2 are displayed in Table 2 for all three settings. The figure shows that E_1 is overall better constrained than E_2. The probability distributions for the second (v_1=0.17 and v_2=0.25) and third (v_1=v_2=0.17) combinations are quite similar as they have a large part of their 95% confidence regions in common. The residual plots obtained with each solution are presented in Fig. 8. All three combinations provide a better fit to the near- and far-field deformation than the one-layer elastic models, but combinations two and three clearly provide the best-fit models. However, since a Poisson's ratio of 0.17 is not realistic for the deeper part of the crust/mantle (see Section 7), our preferred model corresponds to the two-layer elastic model using v_1=0.17 and v_2=0.25. Its good fit is also confirmed by the displacement along the two profiles, as discussed below. Our preferred model estimates the Young's moduli to be E_1=13.9$^{+1.4}_{-1.0}$ GPa and E_2=73.9$^{+8.0}_{-6.6}$ GPa. Residuals for this model lie mostly between -2 and 6 mm in absolute value. East of Síðujökull outlet glacier, some larger residuals occur. A plausible cause for those in the near-field region would be local inaccuracies in the ice model. For the far-field area, the residuals (ranging from -12 to -14 mm) are likely related to atmospheric signal adding some noise to the InSAR observations in this region.

Figure 11 shows the deformation along two profiles (shown in Fig. 8) going from the ice edge at Síðujökull outlet glacier towards the edge of the InSAR scene to the south (profile A) and to the southwest (profile B). The top panels compare the surge-induced displacement ($\mathbf{d}_{surge}$) to the four best-fit model predictions (one one-layer elastic models and three two-layer elastic models) to which we added the ramp and offset estimated during the Bayesian procedure. The lower panels of the figure give the residual displacement along each of the profiles for the four best-fit models. This figure shows that the best prediction of the surge-induced displacement in the near- and far-fields comes from our preferred model with v_1=0.17 and v_2=0.25.

7 DISCUSSION

The time series of interferograms show in detail the crustal deformation at the southwestern edge of Vatnajökull between 1993 and 2002. The signals observed are due to two different processes: the glacial surge that occurred in 1994 at Síðujökull, Skaftárjökull, Tungnaárjökull and Sylgjujökull outlet glaciers, causing LOS lengthening, and the GIA driven by the general retreat of the ice cap over the past 120 years which induces broad LOS shortening. Sources of uncertainty in the InSAR observations include the effects of atmospheric artefacts, unwrapping errors and orbital effects. The first two sources are greatly reduced during the StaMPS analysis and least-squares inversion, with any remaining error considered in the Bayesian approach. The latter uncertainty related to orbits is reduced by estimating and removing a bilinear ramp from the residuals obtained after the comparison between InSAR observations and model results.

Using least squares inversion, we are able to disentangle the signals induced by the surge and the GIA. The method however relies on a number of assumptions. The first assumption is that the 34$\times$19 km area we use at the southwestern corner of the full InSAR scene to estimate the background noise of each interferogram is representative of the full scene. This assumption is reasonable because the area used represents a good portion of the full scene and should sample enough points to obtain a reliable variance of the background noise of the interferograms. Another assumption is that the surge-induced crustal deformation is almost purely elastic. We have validated this assumption through model tests, by comparing outputs from a model with an elastic layer underlain by a viscoelastic layer to those from a one-layer elastic model. The models have identical elastic parameters (E=60 GPa and v=0.25). The viscoelastic test model we used consists of a 20 km thick elastic layer and a viscosity beneath this of 9.3×10^{18} Pa s, according to the best-fit model for the InSAR observations of the ERS track 9 from Auriac et al. (2013). Outputs from the viscoelastic model were taken at different times to evaluate both the short- and long-term responses from the surge. They were then compared to the purely elastic response of the surge. After 6 months, the viscoelastic effect represents less than 1% of the elastic component. On a short-term basis, the results thus show that the influence of the viscoelastic response from the surge is negligible. The crustal response to the surge can therefore be modelled as a step function in time.

The surge-induced crustal deformation signal appears clearly in the LOS deformation map obtained from the least-squares inversion (Fig. 6), reaching a maximum of 75 mm LOS lengthening at the margins of Síðujökull outlet glacier. Our finite element modelling gives three-dimensional displacements and shows that horizontal displacements are nowhere more than 10% of the vertical component, with a maximum near the ice edge. The model LOS change is formed by multiplying the displacement at each pixel with the LOS unit vector. Therefore, the LOS deformation map mostly shows vertical motion of the ground. The observed signal from the surge decays rapidly from the ice cap. Each of the outlet glaciers mapped by our InSAR scene has a specific surge deformation signature, the displacements at Síðujökull and Skaftárjökull outlet glaciers being up to 50 mm greater than those observed on the southern part of Tungnaárjökull. This result is consistent with the ice model (Fig. 2), which predicts less ice being transported to the terminus area of Tungnaárjökull than for Síðujökull and Skaftárjökull. Moreover, the region where ice has been added extends over a larger area at Síðujökull than Tungnaárjökull, increasing the extent of the surge-induced crustal deformation at the margins of Síðujökull compared to Tungnaárjökull.

The GIA uplift rate over the 1993–2002 period estimated from the least-squares inversion reaches 12 mm/yr at the edge of the ice cap east of Síðujökull outlet glacier, relative to the reference area. This result is consistent with those of Auriac et al. (2013) from a 1995–2002 time series. The GIA uplift rate we estimate is assumed to be insensitive to the surge. Two effects linked to the surge could, however, influence the GIA estimate. The first one corresponds to an eventual viscoelastic response of the Earth following the surge. This possibility has been investigated as described above. We found that the viscoelastic response induced by the surge reaches a maximum of 0.9 mm/yr (decreasing away from the ice cap in a similar pattern as the elastic response from the surge), which corresponds to 7.5% of the velocity estimated for the GIA uplift rate in this area during the inversion. Neglecting this effect causes a small underestimate of the uplift velocities induced by the GIA process around Síðujökull, Skaftárjökull, and Tungnaárjökull after the surge. Second, the ice model, with a step advance of ice during the surge, is an oversimplification. Consequently, the GIA uplift rate may be affected by increased ice melting after the surge, as observed after the surge of Bering Glacier, Alaska, in 1993–1995 (Sauber & Molnia 2004). The average summer melting on the highly crevassed ablation areas of the surging outlet glaciers of Vatnajökull ice cap has been observed to increase by $\sim$30% over the 2–3 years after the surge (Björnsson et al. 2003). The resulting deformation, because of the relatively short duration of the increased melting, will be mostly reflected in the elastic response of the crust to the unloading, and therefore has only a limited effect on the long-term GIA uplift. Moreover, since 1995, the mass balance of glaciers in Iceland has been on average negative by $\sim$1 m_{we}/yr, after having been close to zero in the 1980s to the mid-1990s (Björnsson et al. 1998, 2002, 2013). The effect of this increase in melt rate would counteract the small underestimation of the GIA velocities caused by the viscoelastic response from the surge.

Some inaccuracies in the estimate of Poisson’s ratio and Young’s modulus from our Bayesian approach may be caused by assumptions made in the modelling and the statistical method itself. Since we built up our models according to Auriac et al. (2013), the same assumptions stand, i.e. flat Earth, isotropic material, horizontal layering, and no plate spreading. The flat Earth is a reasonable assumption regarding the relatively small size of the surging outlet glaciers. The other assumptions are a simplification of the real Earth. The fact that we assume a uniform value for the Young’s modulus, E, and Poisson’s ratio, v, in one or two layers, means that the estimates we obtain from the Bayesian approach correspond to the average of these parameters for the Icelandic crust/upper mantle. For the two-layer elastic models, we assume a 1-km-thick top layer with a lower value of E than in the underlying layer. This also represents a simplification of the real Earth, which should be better represented by a gradual increase in E with depth, as indicated by seismic studies (Allen et al. 2002). However, results from the comparison between model and observations show that our two-layer models suffice to fit the surge-induced crustal deformation in both the near- and far-field areas. Our results also depend on the assumption made during the Bayesian approach stating that the measurement errors have a multivariate Gaussian distribution. The 95% confidence area obtained with the Bayesian procedure should be interpreted as a formal uncertainty, i.e. a lower estimate of the true uncertainties, as it does not consider eventual model errors.

Uncertainties in the value of E and v also stem from the ice model used in this study, which depends largely on the assumption that the large-scale topographic features on the ice cap did not change shape between the time of acquisitions used to create the DEMs. Comparison of recent surface DEMs of western Vatnajökull (1998 (EMISAR), 2003 and 2010 from SPOT5 HRG and HRS images and LiDAR survey 2010-2012) shows that this assumption is valid for almost all changes in elevation over length scales of 10 km whereas features of less than 1 km in radius are almost randomly scattered. Our ice model may also be influenced by the fact that we assume only a change in ice thickness with no variations in the snow or firn layers or in ice density. When doing DEM differencing over an ice cap, it is common to assume that the snow and firn layers are the same at both times of DEM acquisitions. This is a fair assumption as the snow layer gets renewed by new snow every year and the lower boundaries of the snow and firn layers are constantly transformed into firn and ice, respectively.

As an alternative way to validate our results, we ran the General Inversion for Phase Technique, GIPhT, developed by Feigl & Thurber (2009) and extended by Ali & Feigl (2012), on the surge event that occurred on western Vatnajökull outlet glaciers. We extracted from this method an estimate of the Young's modulus, E=64.0$\pm$6 GPa, and Poisson's ratio, v=0.36± 0.06. Comparison between the best-fit E and v estimated from our one-layer models, our two-layer elastic models, GIPhT approach, and the values found in the literature are summarized in Tables 2 and 3.

The value of Young's modulus estimated from our Bayesian approach with the one-layer models is different to the one inferred from the GIPhT method, likely because each approach tries to fit a different part of the surge-induced signal (see Section 6). The estimates of the static value of the Young's modulus (E_s) we obtain with our two-layer elastic models are however in good agreement with what was inferred by Pinel et al. (2007) and Grapenthin et al. (2006), considering that the values estimated are all averages of the true values over the modelled crustal thickness, and that the Young's modulus is increasing with depth, as demonstrated by seismic studies (Allen et al. 2002) and experimental results (Heap et al. 2011; Asef & Najibi 2013). The values of the Earth parameters estimated by surface load studies are restricted to the volume of Earth significantly influenced by the load variation. To a first approximation, the effects of a surface load depend mostly on Earth properties at depth shallower than the lateral extent of the surface load. It follows that a smaller extent load variation will sample the Young's modulus at shallower levels, which can partly explain the small differences between various studies. Comparison with Young's moduli values derived in Iceland from seismic studies (Pálmason 1971; Gudmundsson 1988; Allen et al. 2002; Hooper et al. 2011) reveals that the dynamic Young's moduli appear larger than the static values, with a smaller difference at larger depth, as expected from experimental studies (e.g., Jizba 1991). This effect has also been observed in other places such as in Hawaii where, at shallow depth ($\sim$2.7 km), E_s was estimated to be five times smaller than E_d (Hooper et al. 2002). Values estimated in Iceland are close to those found at Mount Etna and Hawaii (see Tables 2 and 3). They are, however, much larger than the small value found by Beauducel et al. (2000) for a local study at Merapi volcano. This can be explained by the local estimation performed by these authors by running a model for a very shallow depth.

The estimate of the Poisson's ratio, v=$0.17^{+0.10}_{-0.17}$, inferred from our one-layer models is lower than the v=0.36$\pm$0.06 obtained with the GIPhT approach. This can be explained by the differences in each approach: the different ways to obtain the surge-induced LOS displacements by removing the GIA signal, and the different ways in dealing with the covariance between pixels. The Bayesian approach however shows that the Poisson's ratio parameter is not well constrained by the data, as shown by the 95% confidence region. The low value of v=$0.17^{+0.10}_{-0.17}$ can be partly explained by the fact that Poisson's ratios are highly influenced by the presence of fluids in pores, cracks and fissures in the crust, varying from v=0.27 in drained conditions to v=0.31 for undrained conditions, as estimated by Jónsson et al. (2003). We argue that the surge takes place over a long enough time interval to obtain a drained value of the Poisson's ratio from our results, in which case a Poisson's ratio of v=0.27 falls at the edge of our uncertainties. Moreover, the choice of our preferred model using a Poisson's ratio of v=0.17 for the top layer and v=0.25 underneath has been motivated by the fact that the uppermost kilometre of the Icelandic crust is most likely highly fractured. Although a value of v=0.17 might be too low for the Poisson's ratio of the top layer, we argue that it should be lower than the Poisson's ratio at larger depth. The residual plots demonstrate that such a model manages to resolve most of the surge-induced signal in both near- and far-field areas (Fig. 8).

8 CONCLUSIONS

InSAR has proved to be a powerful tool for mapping the crustal deformation associated with glacial surges. The crustal subsidence signal induced by the studied surge, reaching up to 75 mm in LOS at the edge of Síðujökull outlet glacier, is well resolved right up to the ice margin. The high spatial resolution provided by the InSAR observations also shows the full extent of the surge signal, which decays fast over a $\sim$10 km distance away from the ice cap. The pattern is well reproduced by the finite element modelling. The results show that the surge-induced crustal subsidence signal is composed of two zones: the far-field area, and the near-field area ($\sim$0.5–1 km wide band at the ice margin) which experiences higher deformation. Results from the finite element modelling demonstrate that the one-layer elastic models cannot fully explain both the near- and far-field deformation. The Bayesian approach used to evaluate these models shows that the Poisson's ratio is poorly constrained, with v<0.27. Our preferred model come from the two-layer elastic models, where we use a Poisson's ratio of v_1=0.17 for the upper layer and a Poisson's ratio of v_2=0.25 for the lower layer. As discussed above, these values would indicate drained conditions and a highly fractured top part of the crust around Vatnajökull ice cap. Inferring for the Young's modulus of each layer, we find best-fit values of E_1=12.9–15.3 GPa and E_2=67.3–81.9 GPa for the upper and lower layers, respectively (95% confidence intervals). Residuals are small and demonstrate that the models can accommodate for both the near- and far-field deformation. Our results are consistent with other studies, given that the depth at which it is possible to resolve for the Earth parameters is dependent on the spatial extent of the load at the surface.

ACKNOWLEDGMENTS

This study was funded by a Ph.D. grant to Amandine Auriac and support to Freysteinn Sigmundsson from the University of Iceland Research Fund, the Icelandic Research Fund (Volcano Anatomy Project), and EU project FUTUREVOLC. Research was partially supported by a grant from the U.S. National Science Foundation (EAR-0810134) and the National Aeronautics and Space Administration (NASA-NNX12AO37G). Synthetic Aperture Radar data from the SAR and ASAR sensors from the ERS and Envisat satellite missions operated by the European Space Agency (ESA) were used under the terms and conditions of several Category-I projects awarded to F. Sigmundsson, K. Feigl and A. Hooper. We thank Jeanne Sauber and an anonymous reviewer for their valuable comments and suggestions for the improvement of the manuscript. The figures were created using the GMT software package (Wessel & Smith 1998).

REFERENCES

ABAQUS, 2009. ABAQUS manuals, version 6.9, *SIMULIA*.

Ali, S. T. & Feigl, K., 2012. A new strategy for estimating geophysical parameters from InSAR data: Application to the Krafla central volcano in Iceland, *Geochemistry, Geophysics, Geosystems*, **13**(4), http://onlinelibrary.wiley.com/journal/10.1002/

Allen, R. M., Nolet, G., Morgan, W. J., Vogfjörd, K., Nettles, M., Ekström, G., Bergsson, B. H., Erlendsson, P., Foulger, G. R., Jakobsdóttir, S., Julian, B. R., Pritchard, M., Ragnarsson, S., & Stefánsson, R., 2002. Plume-driven plumbing and crustal formation in Iceland, *Journal of Geophysical Research*, **107**(B8), 19.

Árnadóttir, T., Lund, B., Jiang, W., Geirsson, H., Björsson, H., Einarsson, P., & Sigurdsson, T., 2009. Glacial rebound and plate spreading: results from the first countrywide GPS observations in Iceland, *Geophysical Journal International*, **177**, 691–716.

Asef, M. R. & Najibi, A. R., 2013. The effect of confining pressure on elastic wave velocities and dynamic to static Young's modulus ratio, *Geophysics*, **78**(3), 8.

Auriac, A., Spaans, K. H., Sigmundsson, F., Hooper, A., Schmidt, P., & Lund, B., 2013. Iceland rising: Solid Earth response to ice retreat inferred from satellite radar interferometry and viscoelastic modeling, *Journal of Geophysical Research*, **118**, 14.

Beauducel, F., Cornet, F.-H., Suhanto, E., Duquesnoy, T., & Kasser, M., 2000. Constraints on magma flux from displacements data at Merapi volcano, Java, Indonesia, *Journal of Geophysical Research*, **105**(B4), 8193–8203.

Björnsson, H., 1978. The surface area of glaciers in Iceland, *Jökull*, **28**, 31.

Björnsson, H. & Pálsson, F., 1991. Vatnajökull, northeastern part, 1:100,000, 8 maps, *University of Iceland and Landsvirkjun*.

Björnsson, H., Pálsson, F., & Guðmundsson, M. T., 1992. Vatnajökull, northwestern part, 1:100,000, 8 maps, *University of Iceland and Landsvirkjun*.

Björnsson, H., Pálsson, F., Gudmundsson, M. T., & Haraldsson, H. H., 1998. Mass balance of western and northern Vatnajökull, Iceland, 1991-1995, *Jökull*, **45**, 35–58.

Björnsson, H., Pálsson, F., & Haraldsson, H. H., 2002. Mass balance of Vatnaökull (1991-2001) and Langjökull (1996-2001), Iceland, *Jökull*, **51**, 75–78.

Björnsson, H., Pálsson, F., Sigurðsson, O., & Flowers, G. E., 2003. Surges of glaciers in Iceland, *Annals of Glaciology*, **36**, 82–90.

Björnsson, H., Pálsson, F., Gudmundsson, S., Magnússon, E., Adalgeirsdóttir, G., Jóhannesson, T., Berthier, E., Sigurðsson, O., & Thorsteinsson, T., 2013. Contribution of Icelandic ice caps to sea level rise: Trends and variability since the Little Ice Age, *Geophysical Research Letters*, **40**, 1546–1550.

Cheng, C. H. & Johnston, D. H., 1981. Dynamic and static moduli, *Geophysical research letters*, **8**(1), 39–42.

Currenti, G., Del Negro, C., & Ganci, G., 2007. Modelling of ground deformation and gravity fields using finite element method: an application to Etna volcano, *Geophysical Journal International*, **169**, 775–786.

Einarsson, P. & Saemundsson, K., 1987. Earthquake epicenters 1982-1985 and volcanic systems in Iceland (map), *Í Hlutarsins Eðli: Festschrift for Thorbjorn Sigurgeirsson*.

Eissa, E. A. & Kazi, A., 1988. Relation between static and dynamic Young's moduli of rocks, *International Journal of Rocks Mechanics and Mining Sciences & Geomechanics Abstracts*, **25**(6), 479–482.

Feigl, K. & Thurber, C. H., 2009. A method for modelling radar interferograms without phase unwrapping: application to the M 5 Fawnshin, California earthquake of 1992 December 4, *Geophysical Journal International*, **176**(2), 491–504.

Grapenthin, R., Sigmundsson, F., Geirsson, H., Árnadóttir, T., & Pinel, V., 2006. Icelandic rhytmics: annual modulation of land elevation and plate spreading by snow load, *Geophysical Research Letters*, **33**.

Gudmundsson, A., 1988. Effect of tensile stress concentration around magma chambers on intrusion and extrusion frequencies, *Journal of Volcanology and Geothermal Research*, **35**, 179–194.

Heap, M., Baud, P., Meredith, P., Vinciguerra, S., Bell, A., & Main, I., 2011. Brittle creep in basalt and its application to time-dependent volcano deformation, *Earth and Planetary Science Letters*, **307**, 71–82.

Hooper, A., 2008. A multi-temporal InSAR method incorporating both persistent scatterer and small baseline approaches, *Geophysical Research Letters*, **35**.

Hooper, A., Segall, P., Johnson, K., & Rubinstein, J., 2002. Reconciling seismic and geodetic models of the 1989 Kilauea south flank earthquake, *Geophysical Research Letters*, **29**(22), 4.

Hooper, A., Ófeigsson, B., Sigmundsson, F., Lund, B., Einarsson, P., Geirsson, H., & Sturkell, E., 2011. Increased capture of magma in the crust promoted by ice-cap retreat in Iceland, *Nature Geoscience*.

Hooper, A., Pietrzak, J., Simons, W. Cui, H., Riva, R., Naeije, M., Terwisscha van Scheltinga, A., Schrama, E., Stelling, G., & Socquet, A., 2013. Importance of horizontal seafloor motion on tsunami height for the 2011 Mw=9.0 Tohoku-Oki earthquake, *Earth and Planetary Science Letters*, **361**, 469–479.

Jizba, D. L., 1991. *Mechanical and Acoustical Properties of Sandstones and Shales*, Ph.D. thesis, Stanford University.

Jónsson, S., Segall, P., Pedersen, R., & Björnsson, G., 2003. Post-earthquake ground movements correlated to pore-pressure transients, *Nature*, **424**, 179–183.

Kampes, B. & Usai, S., 1999. Doris: the Delft Object-oriented Radar Interferometric Software, *2nd International Symposium on Operationalization of Remote Sensing*, Enschede, The Netherlands.

Magnússon, E., Björnsson, H., Pálsson, F., & Dall, J., 2004. Glaciological application of InSAR topography data of western Vatnajökull acquired in 1998, *Jökull*, pp. 17–36.

Pagli, C., Sigmundsson, F., Lund, B., Sturkell, E., Geirsson, H., Einarsson, P., Árnadóttir, T., & Hreinsdóttir, S., 2007. Glacio-isostatic deformation around the Vatnajökull ice cap, Iceland, induced by recent climate warming: GPS observations and finite element modeling, *Journal of Geophysical Research*, **112**.

Pálmason, G., 1971. *Crustal structure of Iceland from explosion seismology*, Societas Scientiarum Islandica.

Pinel, V., Sigmundsson, F., Sturkell, E., Geirsson, H., Einarsson, P., Gudmundsson, M. T., & Högnadóttir, T., 2007. Discriminating volcano deformation due to magma movements and variable surface loads: application to Katla subglacial volcano, Iceland, *Geophysical Journal International*, **169**, 325–338.

Rosen, P. A., Hensley, S., & Peltzer, G., 2004. Updated Repeat Orbit Interferometry Package Released, *EOS Trans. AGU*, **85**(5), 47.

Sauber, J. M. & Molnia, B. F., 2004. Glacier ice mass fluctuations and fault instability in tectonically active Southern Alaska, *Global and Planetary Change*, **42**, 279–293.

Thorarinsson, S., 1969. Glacier surges in Iceland, with special reference to the surges of Brúarjökull, *Canadian Journal of Earth Sciences*, **6**, 875–882.

Wessel, P. & Smith, W. H. F., 1998. New, improved version of generic mapping tools released, *Eos, Transactions American Geophysical Union*, **79**(47), 579–579.

This paper has been produced using the Blackwell Scientific Publications GJI LaTeX2e class file.

LIST OF TABLES

Table 1 Overview of the SAR acquisitions from the ERS satellite, track 9, used in this study. Perpendicular baselines relative to the acquisition on 17 September 1996 are shown.

Table 2 Overview of the elastic Earth parameters inferred from previous studies in Iceland and this study.

Table 3 Overview of the elastic Earth parameters inferred from previous studies at Etna, Merapi and Kilauea volcanoes.

LIST OF FIGURES

Fig. 1 (a) Ice caps and tectonic setting of Iceland. Fissure swarms are shown in light yellow and central volcanoes with their associated calderas are represented by oval outlines (after Einarsson & Saemundsson 1987) . The Eastern Volcanic Zone (EVZ) is displayed in blue. Main ice caps names are indicated in red (D.: Drangajökull, S.: Snæfelsjökull, L.: Langjökull, M.: Mýrdalsjökull, H.: Hofsjökull, and V.: Vatnajökull). The color boxes show the area spanned by our InSAR data: red for the full scene and blue for the cropped one. The black box gives the area shown in (b). (b) Zoom in the southwestern region of Vatnajökull, with the names of the four surging outlet glaciers studied here (Sy.: Sylgjujökull, Tu.: Tungnaárjökull, Sk.: Skaftárjökull and Sí.: Síðujökull) and the cropped InSAR scene outlines (blue box).

Fig. 2 Surface elevation change at Sylgjujökull (Sy.), Tungnaárjökull (Tu.), Skaftárjökull (Sk.) and Síðujökull (Sí.) outlet glaciers between 1993 and 1995. Negative values indicate an ice loss while positive values indicate a gain in ice.

Fig. 3 Connections (black lines) between individual InSAR acquisitions (red dots) forming the 65 highly coherent small-baseline interferograms used in the study. The y-axis displays the perpendicular baseline between each image and an arbitrary master image on 17 september 1996.

Fig. 4 Interferograms spanning 31 July 1993 to 19 June 1995, showing the surge at Tungnaárjökull (Tu.), Skaftárjökull (Sk.) and Síðujökull (Sí.) outlet glaciers. The black and grey arrows show the azimuth of the satellite and the look direction, respectively. (a) Wrapped interferogram showing the deformation in fringes between $\pm\pi$. One full fringe (2π) equals 28.3 mm deformation. (b) Unwrapped interferogram. The black star designates the reference area and negative values indicate LOS lengthening.

Fig. 5 Single-master time series created from the 65 small baseline interferograms, spanning 1993 to 2002. The deformation shown is in LOS (negative values for LOS lengthening), relative to the reference area indicated by the black star. Each panel shows the cumulative change from the first interferogram on 26 June 1993, where Tu., Sk. and Sí. indicate Tungnaárjökull, Skaftárjökull and Síðujökull, respectively. The color scale has been modified such that points from -80 mm to -120 mm appear in the same color, to enhance the viewing of the surge signal.

Fig. 6 Inferred deformation signals from the linear inversion ran on the single-master time series: (a) GIA signal estimated as a continuous velocity, in mm/yr, (b) surge displacement estimated as a step function, in mm. Both results are shown in LOS and with respect to the reference area, where negative values stand for LOS lengthening (note the difference in color scaling). The black and grey arrows show the azimuth of the satellite and the look direction, respectively. Tu., Sk. and Sí. indicate Tungnaárjökull, Skaftárjökull and Síðujökull outlet glaciers, respectively.

Fig. 7 Vertical deformation observed at a randomly chosen mesh node as a function of Young's modulus. The red circles show results from the finite element models run with E=20, 60 and 90 GPa. The blue line gives the vertical deformation calculated with the finite element model result using E=20 GPa and scaling it for the different values of E, according to Hooke's law. The dashed green line, superimposed on the blue one, represents the deformation calculated with the Green's function approach using E=40 GPa, and scaled to other values of E using Hooke's law.

Fig. 8 Top row: (a) Referenced LOS surge displacement estimated from the InSAR data (output from the least-squares inversion minus the ramp and offset estimated from the Bayesian approach), (b) best-fit one-layer elastic model (E=46.4 GPa and v=0.17) converted to LOS, and (c) residual between (a) and (b), respectively. Rows 2–4 show similar set of panels for the other models. (d), (e) and (f) Same as above but with the two-layer elastic best-fit model with v_1=v_2=0.25, E_1=12.9 GPa, and E_2=70.5 GPa. (g) (h) and (i) Same as above with v_1=0.17, E_1=12.9 GPa, v_2=0.25 and E_2=73.9 GPa. (j), (k) and (l) Same as above with v_1=v_2=0.17, E_1=12.8 GPa, and E_2=76.2 GPa. Tu., Sk. and Sí. indicate Tungnaárjökull, Skaftárjökull and Síðujökull outlet glaciers, respectively. The black and grey arrows show the azimuth of the satellite and the look direction, respectively. The black lines locate the profiles A and B presented in Fig. 11. Note the difference in scale between plots (a) to (c) from the one-layer elastic models and plots (d) to (l) from the two-layer elastic models.

Fig. 9 Probability distribution estimate of the Young's modulus (E) and Poisson's ratio (v) for one-elastic layer models. The best model (white cross) predicts E=46.4 GPa and v=0.17. The black outline shows the 95% confidence region, located between 43.2–49.7 GPa for E and 0–0.27 for v, the black dashed line gives the 68% confidence region.

Fig. 10 Probability distribution estimates of the Young's moduli for the upper (E_1) and lower (E_2) layers for the two-layer elastic models. The plus symbols indicate the best-fit models in each case, the continuous outlines the 95% confidence regions, and the dashed lines the 68% confidence regions. In green, we show the distribution for the models with v_1=v_2=0.25, indicating a best-fit model of E_1=12.9$^{+1.3}_{-1.0}$ GPa and E_2=70.5$^{+7.0}_{-6.0}$ GPa. In red, we show the results for our preferred model with v_1=0.17 and v_2=0.25, giving a best estimate of E_1=13.9$^{+1.4}_{-1.0}$ GPa and E_2=73.9$^{+8.0}_{-6.6}$ GPa. Results for the models with v_1=v_2=0.17 are shown in blue and predict a best-fit model of E_1=13.8$^{+1.3}_{-1.0}$ GPa and E_2=76.2$^{+8.4}_{-6.9}$ GPa. The uncertainties given here correspond to the 95% confidence regions. The color scale shows the probability distribution for our preferred model.

Fig. 11 Plots showing the deformation along two profiles (location on Fig. 8). Results from profile A are displayed on the left side panels and results from profile B are shown in the right side panels. (a) and (b) Comparison between the surge displacement field (corresponding to $\mathbf{d}_{surge}$) and the best-fit models (where we added the ramp and offset estimated by the Bayesian approach), in black and coloured symbols respectively. (c) and (d) Residual displacement along each profile for each of the best-fit models. In all four panels, purple circles indicate the results obtained with the best-fit one-layer model, the green triangles are used for the best-fit two-layer model with v_1=v_2=0.25, the red squares correspond to the best-fit two-layer model with v_1=0.17 and v_2=0.25 (preferred model), and the blue inverted triangles show the best-fit two-layer model with v_1=v_2=0.17.

Table 1.

Acquisition date [yyyy–mm–dd]	**Perpendicular baseline [m]**
1993–06–26	-318
1993–07–31	-88
1993–09–04	174
1993–10–09	318
1995–06–19	-184
1995–08–28	152
1995–08–29	151
1995–10–02	269
1995–10–03	506
1996–06–04	-231
1996–07–09	394
1996–08–13	202
1996–09–17	0
1997–06–24	16
1997–07–29	109
1997–09–02	491
1998–07–14	-511
1998–08–18	-333
1998–09–22	125
1999–08–03	342
1999–09–07	-601
2000–08–22	119
2002–07–23	92

Table 2.

Poisson's ratio[1]	Static Young's modulus E_s [GPa]	Dynamic Young's modulus E_d [GPa]	Elastic Depth [km]	Source
$0.17^{+0.10}_{-0.17}$	$46.4^{+3.3}_{-3.2}$		∼half-space	This study (one-layer elastic model)
0.36±0.06	64±6		half-space	This study using GIPhT method (Feigl & Thurber 2009; Ali & Feigl 2012)
(v_1=0.25 / v_2=0.25)	E_1=$12.9^{+1.3}_{-1.0}$ / E_2=$70.5^{+7.0}_{-6.0}$		1 km / ∼half-space	This study (two-layer elastic model)
(v_1=0.17 / v_2=0.25)	E_1=$13.9^{+1.4}_{-1.0}$ / E_2=$73.9^{+8.0}_{-6.6}$		1 km / ∼half-space	This study (two-layer preferred model)
(v_1=0.17 / v_2=0.17)	E_1=$13.8^{+1.3}_{-1.0}$ / E_2=$76.2^{+8.4}_{-6.9}$		1 km / ∼half-space	This study (two-layer elastic model)
(0.25)	29±5		half-space	Pinel et al. (2007)
(0.25)	40±15		half-space	Grapenthin et al. (2006)
(0.27)		45.7	0–1	Hooper et al. (2011), derived from seismic data by Allen et al. (2002)
		58.4	1–3	
		76.2	3–5	
		94.0	5–7	
		111.8	7–	
(0.25)		14.4	0–0.5	Gudmundsson (1988), derived from seismic data by Pálmason (1971)
		37.1	0.5–1	
		57.4	1–2.2	
		102	2.2–5.5	
		134	5.5–	

[1] Values in brackets indicate an assumed value for this parameter, instead of inferred ones.

Table 3.

Poisson's ratio[2]	Static Young's modulus E_s [GPa]	Dynamic Young's modulus E_d [GPa]	Elastic thickness [km]	Source
0.26	17.9–21.1	25.5		Heap et al. (2011)
(0.25)		11.5	0–1	Currenti et al. (2007)
		28.8	1–5	
		63	5–8	
		86	8–15	
		101	15–23	
		133	23–50	
(0.25)	11.25		2.7	Hooper et al. (2002)
(0.25)	0.7±0.2			Beauducel et al. (2000)

[2] Values in brackets indicate an assumed value for this parameter, instead of inferred ones.

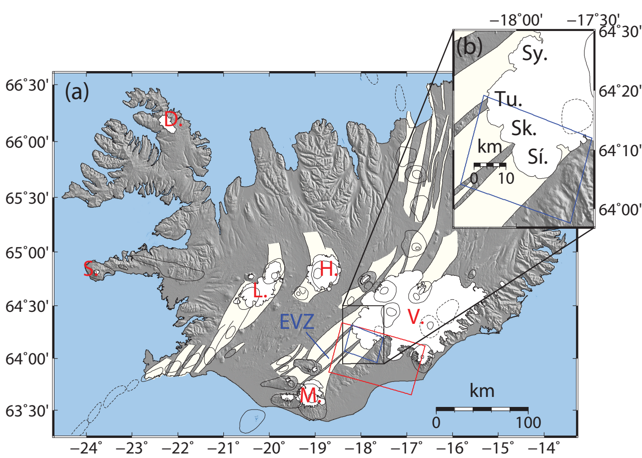

Figure 1. (a) Ice caps and tectonic setting of Iceland. Fissure swarms are shown in light yellow and central volcanoes with their associated calderas are represented by oval outlines (after Einarsson & Saemundsson 1987) . The Eastern Volcanic Zone (EVZ) is displayed in blue. Main ice caps names are indicated in red (D.: Drangajökull, S.: Snæfelsjökull, L.: Langjökull, M.: Mýrdalsjökull, H.: Hofsjökull, and V.: Vatnajökull). The color boxes show the area spanned by our InSAR data: red for the full scene and blue for the cropped one. The black box gives the area shown in (b). (b) Zoom in the southwestern region of Vatnajökull, with the names of the four surging outlet glaciers studied here (Sy.: Sylgjujökull, Tu.: Tungnaárjökull, Sk.: Skaftárjökull and Sí.: Síðujökull) and the cropped InSAR scene outlines (blue box).

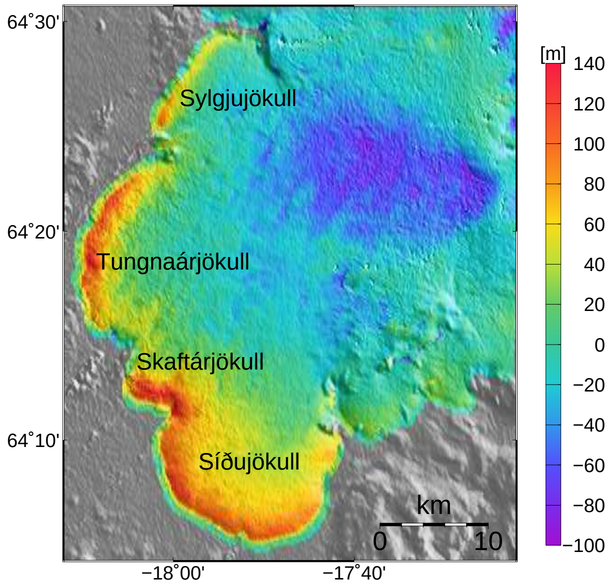

Figure 2. Surface elevation change at Sylgjujökull (Sy.), Tungnaárjökull (Tu.), Skaftárjökull (Sk.) and Síðujökull (Sí.) outlet glaciers between 1993 and 1995. Negative values indicate an ice loss while positive values indicate a gain in ice.

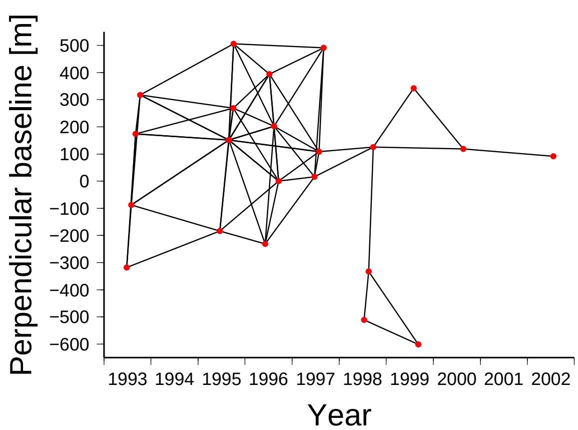

Figure 3. Connections (black lines) between individual InSAR acquisitions (red dots) forming the 65 highly coherent small-baseline interferograms used in the study. The y-axis displays the perpendicular baseline between each image and an arbitrary master image on 17 september 1996.

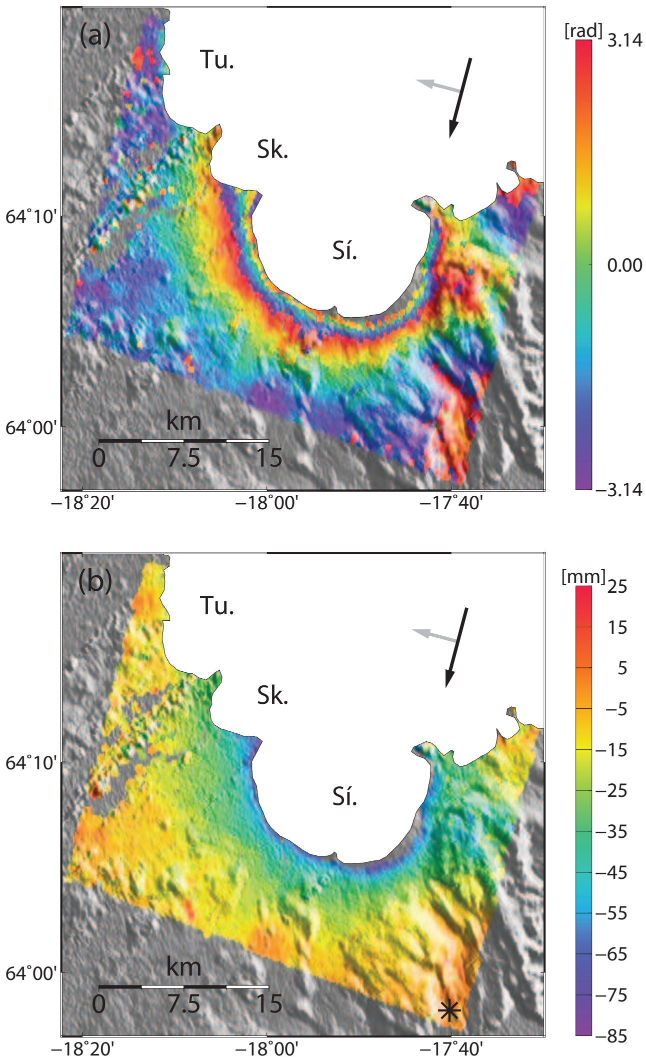

Figure 4. Interferograms spanning 31 July 1993 to 19 June 1995, showing the surge at Tungnaárjökull (Tu.), Skaftárjökull (Sk.) and Síðujökull (Sí.) outlet glaciers. The black and grey arrows show the azimuth of the satellite and the look direction, respectively. (a) Wrapped interferogram showing the deformation in fringes between $\pm\pi$. One full fringe (2π) equals 28.3 mm deformation. (b) Unwrapped interferogram. The black star designates the reference area and negative values indicate LOS lengthening.

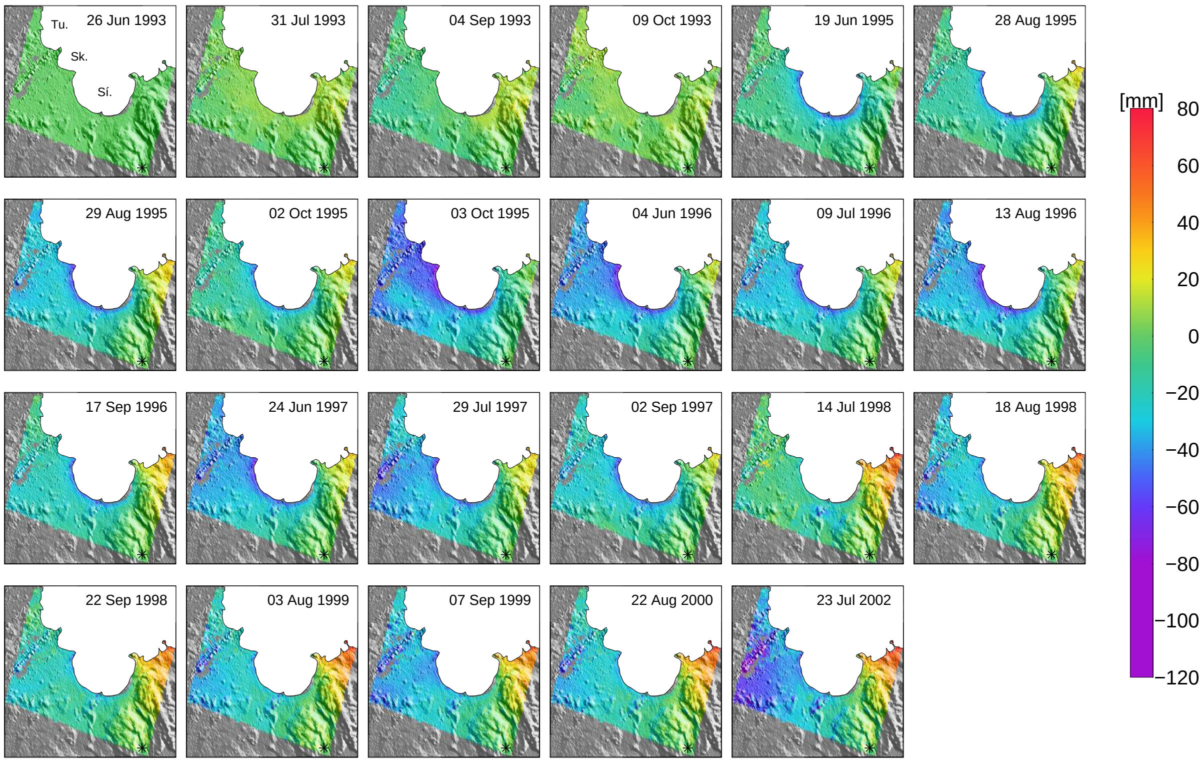

Figure 5. Single-master time series created from the 65 small baseline interferograms, spanning 1993 to 2002. The deformation shown is in LOS (negative values for LOS lengthening), relative to the reference area indicated by the black star. Each panel shows the cumulative change from the first interferogram on 26 June 1993, where Tu., Sk. and Sí. indicate Tungnaárjökull, Skaftárjökull and Síðujökull, respectively. The color scale has been modified such that points from -80 mm to -120 mm appear in the same color, to enhance the viewing of the surge signal.

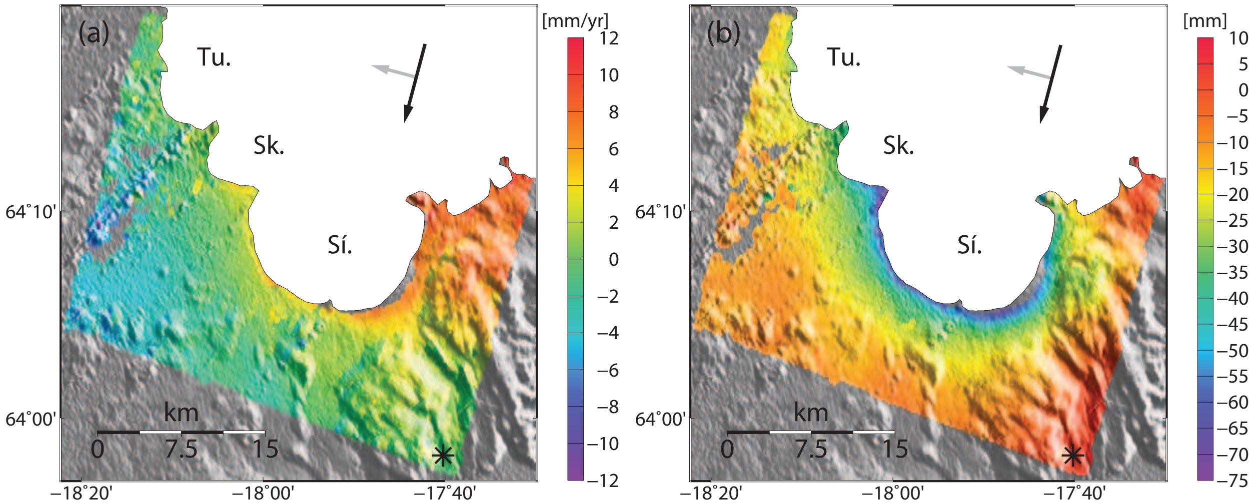

Figure 6. Inferred deformation signals from the linear inversion ran on the single-master time series: (a) GIA signal estimated as a continuous velocity, in mm/yr, (b) surge displacement estimated as a step function, in mm. Both results are shown in LOS and with respect to the reference area, where negative values stand for LOS lengthening (note the difference in color scaling). The black and grey arrows show the azimuth of the satellite and the look direction, respectively. Tu., Sk. and Sí. indicate Tungnaárjökull, Skaftárjökull and Síðujökull outlet glaciers, respectively.

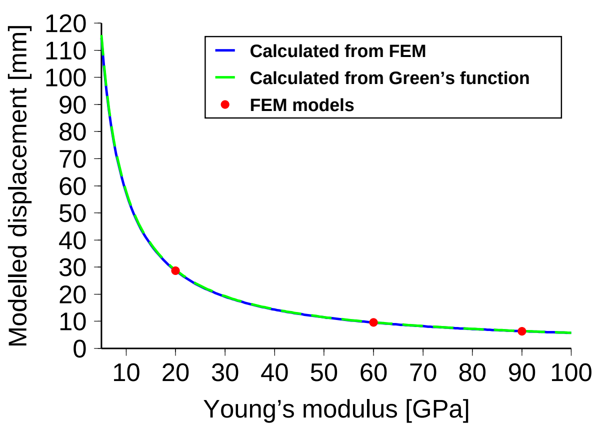

Figure 7. Vertical deformation observed at a randomly chosen mesh node as a function of Young's modulus. The red circles show results from the finite element models run with E=20, 60 and 90 GPa. The blue line gives the vertical deformation calculated with the finite element model result using E=20 GPa and scaling it for the different values of E, according to Hooke's law. The dashed green line, superimposed on the blue one, represents the deformation calculated with the Green's function approach using E=40 GPa, and scaled to other values of E using Hooke's law.

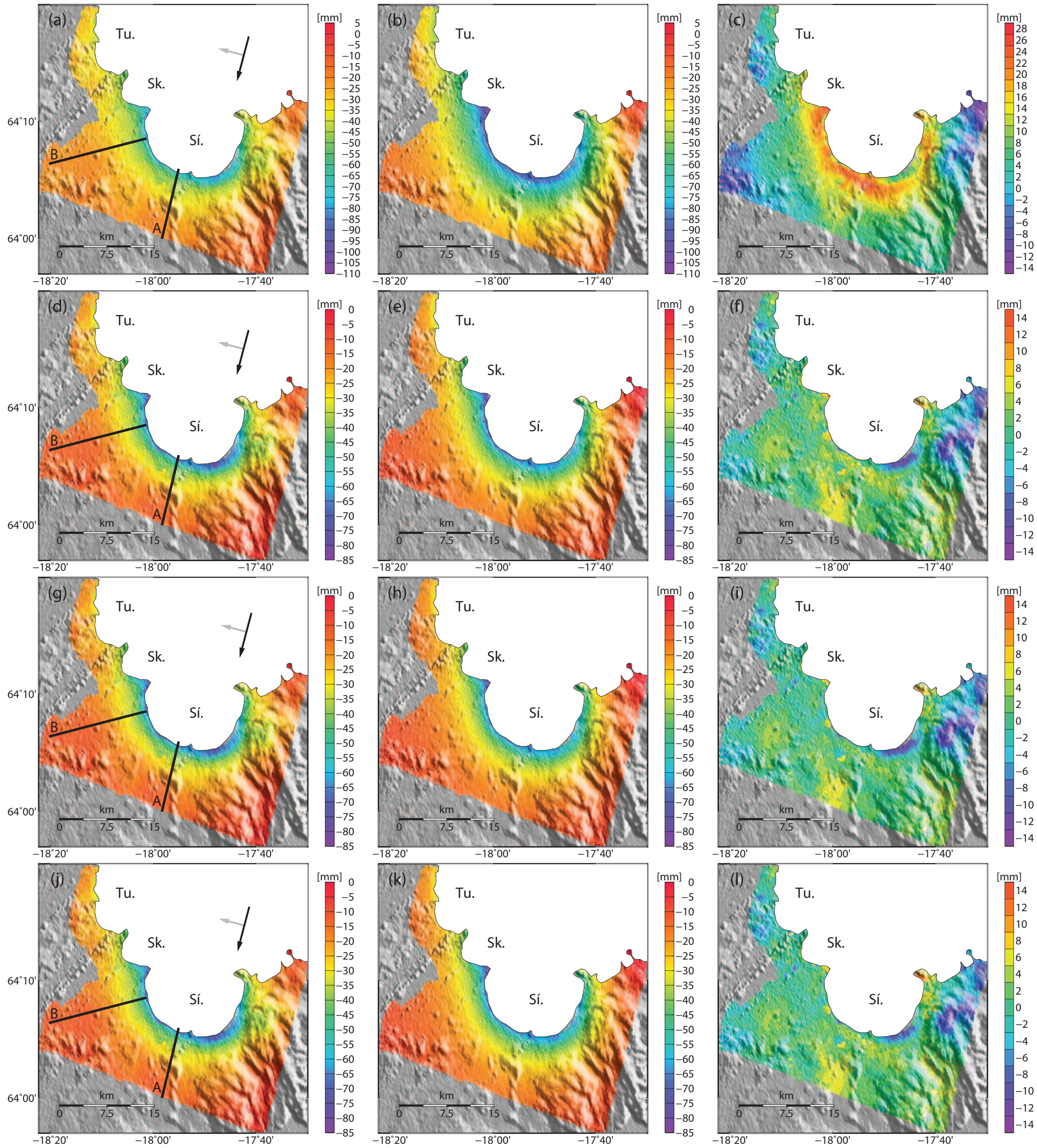

Figure 8. Top row: (a) Referenced LOS surge displacement estimated from the InSAR data (output from the least-squares inversion minus the ramp and offset estimated from the Bayesian approach), (b) best-fit one-layer elastic model (E=46.4 GPa and ν=0.17) converted to LOS, and (c) residual between (a) and (b), respectively. Rows 2–4 show similar set of panels for the other models. (d), (e) and (f) Same as above but with the two-layer elastic best-fit model with ν_1=ν_2=0.25, E_1=12.9 GPa, and E_2=70.5 GPa. (g) (h) and (i) Same as above with ν_1=0.17, E_1=12.9 GPa, ν_2=0.25 and E_2=73.9 GPa. (j), (k) and (l) Same as above with ν_1=ν_2=0.17, E_1=12.8 GPa, and E_2=76.2 GPa. Tu., Sk. and Sí. indicate Tungnaárjökull, Skaftárjökull and Síðujökull outlet glaciers, respectively. The black and grey arrows show the azimuth of the satellite and the look direction, respectively. The black lines locate the profiles A and B presented in Fig. 11. Note the difference in scale between plots (a) to (c) from the one-layer elastic models and plots (d) to (l) from the two-layer elastic models.

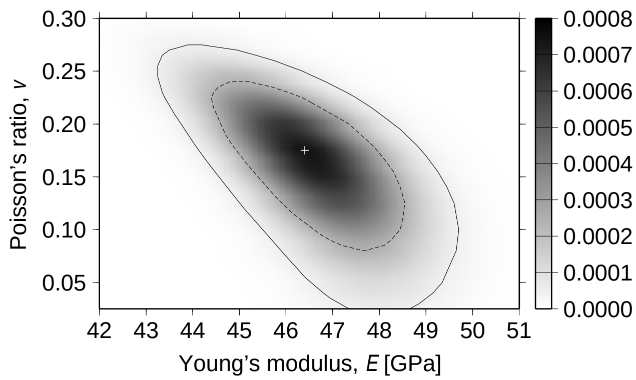

Figure 9. Probability distribution estimate of the Young's modulus (E) and Poisson's ratio (v) for one-elastic layer models. The best model (white cross) predicts E=46.4 GPa and v=0.17. The black outline shows the 95% confidence region, located between 43.2–49.7 GPa for E and 0–0.27 for v, the black dashed line gives the 68% confidence region.

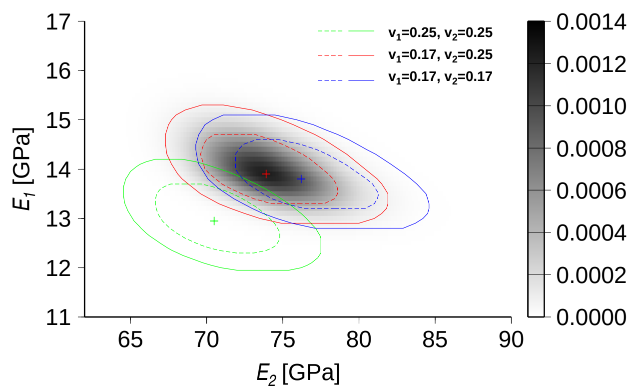

Figure 10. Probability distribution estimates of the Young's moduli for the upper (E_1) and lower (E_2) layers for the two-layer elastic models. The plus symbols indicate the best-fit models in each case, the continuous outlines the 95% confidence regions, and the dashed lines the 68% confidence regions. In green, we show the distribution for the models with v_1=v_2=0.25, indicating a best-fit model of E_1=$12.9^{+1.3}_{-1.0}$ GPa and E_2=$70.5^{+7.0}_{-6.0}$ GPa. In red, we show the results for our preferred model with v_1=0.17 and v_2=0.25, giving a best estimate of E_1=$13.9^{+1.4}_{-1.0}$ GPa and E_2=$73.9^{+8.0}_{-6.6}$ GPa. Results for the models with v_1=v_2=0.17 are shown in blue and predict a best-fit model of E_1=$13.8^{+1.3}_{-1.0}$ GPa and E_2=$76.2^{+8.4}_{-6.9}$ GPa. The uncertainties given here correspond to the 95% confidence regions. The color scale shows the probability distribution for our preferred model.

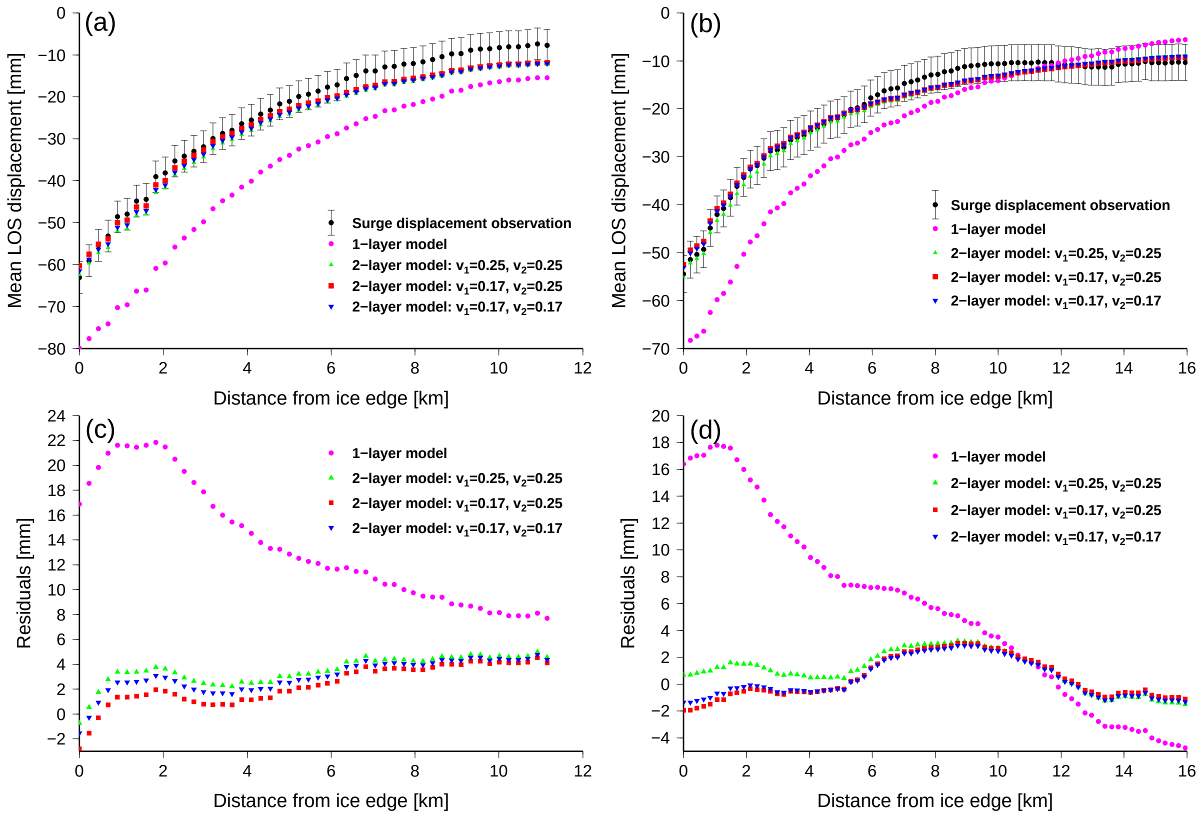

Figure 11. Plots showing the deformation along two profiles (location on Fig. 8). Results from profile A are displayed on the left side panels and results from profile B are shown in the right side panels. (a) and (b) Comparison between the surge displacement field (corresponding to $\mathbf{d}_{surge}$) and the best-fit models (where we added the ramp and offset estimated by the Bayesian approach), in black and coloured symbols respectively. (c) and (d) Residual displacement along each profile for each of the best-fit models. In all four panels, purple circles indicate the results obtained with the best-fit one-layer model, the green triangles are used for the best-fit two-layer model with v_1=v_2=0.25, the red squares correspond to the best-fit two-layer model with v_1=0.17 and v_2=0.25 (preferred model), and the blue inverted triangles show the best-fit two-layer model with v_1=v_2=0.17.